







Exploring the impact of Cr-doping on the crystallographic and magnetic structure of Mn_5Si_3 antiferromagnetic alloy

Sanat Kumar Adhikari,¹ Riya Roy,¹ Mohamad Numan ,² Ashok Das,³ Rosni Roy,¹ Sambhu Charan Das ,^{1,4} Jhuma Sannigrahi ,⁵ Sabyasachi Pramanick,¹ Kalyanashis De,⁶ Qiang Zhang ,⁷ Sergiu Levchenko,⁸ Edmund Welter,⁸ Sudipta Bandyopadhyay ,³ Rajib Mondal,¹ and Souvik Chatterjee ,^{1,*}

¹UGC-DAE Consortium for Scientific Research, Kolkata Centre, Sector III, LB-8, Salt Lake, Kolkata 700 106, India

²School of Physical Sciences, Indian Association for the Cultivation of Science, 2 A and B Raja S. C. Mullick Road, Jadavpur, Kolkata 700 032, India

³Department of Physics, University of Calcutta, 92 A.P.C. Road, Kolkata 700009, India

⁴Department of Physics, Tamkang University, New Taipei City 251, Taiwan

⁵School of Physical Sciences, Indian Institute of Technology Goa, Ponda 403401, Goa, India

⁶School of Science and Technology, The Neotia University, South 24 Parganas 743368, India

⁷Neutron Science Division, Oak Ridge National Laboratory, Oak Ridge, Tennessee 37831, USA

⁸Deutsches Elektronen-Synchrotron DESY, Notkestraße 85, 22607 Hamburg, Germany



(Received 20 March 2024; accepted 20 May 2024; published 7 June 2024)

The role of Cr-doping on the structural and magnetic ground states of Mn_5Si_3 alloy has been investigated through temperature-dependent neutron powder diffraction (NPD) and x-ray absorption fine structure (XAFS) techniques. All the Cr-doped alloys of nominal composition $\text{Mn}_{5-x}\text{Cr}_x\text{Si}_3$ (for $x = 0.05, 0.1, \text{ and } 0.2$) undergo two first-order magnetostructural phase transitions, i.e., hexagonal (space group $P6_3/mcm$) paramagnetic \rightarrow orthorhombic (space group $Ccmm$) collinear antiferromagnetic \rightarrow orthorhombic (space group $Cc2m$) noncollinear antiferromagnetic phase, on cooling from room temperature. NPD studies at different constant temperatures indicate that both antiferromagnetic phases are commensurate in nature and can be represented by the $q = (0, 1, 0)$ magnetic propagation vector for all the Cr-doped alloys. Such doping at the Mn site results in a significant modification of the noncollinear antiferromagnetic structure (both moment size and orientation) and hence affects the unusual magnetic properties, such as inverted hysteresis loop, thermomagnetic irreversibility, etc. The XAFS measurements were performed to interpret the local environment of doped Cr atoms in detail, which is critical for a microscopic understanding of the unusual properties of this class of Cr-doped Mn_5Si_3 alloys. The analysis confirms the elemental state of Cr in the doped alloys and indicates a high degree of preservation of local crystallographic structure with varying Cr concentration and sample temperature. Doping induces intriguing changes in XAFS patterns, elucidated through different types of scattering mechanisms associated with the central absorbing Cr atom.

DOI: [10.1103/PhysRevMaterials.8.064405](https://doi.org/10.1103/PhysRevMaterials.8.064405)

I. INTRODUCTION

Among various members of the metal silicide family, Mn_5Si_3 has attracted renewed attention among researchers not only for its possible application in the field of microelectronics, but also for the recent observation of interesting magnetic properties, such as the anomalous Hall effect (AHE), inverted hysteresis loop (IHL), thermomagnetic irreversibility (TI), large inverse magnetocaloric effect, spin fluctuations, etc. [1–14]. Several doping strategies have been adopted to check the robustness of the observed unusual magnetic features [6, 15–21]. At room temperature (T), the pristine Mn_5Si_3 alloy is paramagnetic (PM) in nature and crystallizes in a $D8_8$ -type hexagonal structure (space group $P6_3/mcm$). On cooling from room temperature, it undergoes two magnetostructural transitions: (i) hexagonal PM to orthorhombic (space group

$Ccmm$) collinear antiferromagnetic (AFM2) transition at 100 K, and (ii) orthorhombic (space group $Ccmm$) AFM2 to orthorhombic (space group $Cc2m$) noncollinear antiferromagnetic (AFM1) transition at 66 K [1–5, 7–13]. Moreover, an additional noncollinear antiferromagnetic phase (AFM1') in the presence of an external magnetic field (H) has also been reported by Sürgers *et al.* [1]. Previous x-ray and neutron powder diffraction (NPD) data confirm the presence of multiple crystallographic sites for Mn in all three phases. Different magnetic moment values at different Mn sites (particularly in the AFM1 phase) play a decisive role in the observed exotic magnetic behaviors.

Foreign element doping at different sites of the Mn_5Si_3 alloy results in a modification of the nearest-neighbor Mn-Mn distance [6, 15–21]. Such modification directly affects the magnetic behavior due to the near-critical values of Mn-Mn nearest-neighbor distance of the pure Mn_5Si_3 alloy. Recent studies by our group on the Ni/Co/Cr-doped alloys reveal the gradual disappearance of IHL and TI properties with in-

*souvik@csr.res.in; souvikchat@gmail.com

creasing doping concentration and the disappearance of the AFM1' phase was found to be primarily responsible for such behavior [6,15,16,19]. Though several doping studies have been performed (mostly magnetic and electrical studies), the substitution of the host atom by the dopant has not yet been confirmed. Recently, our group reported the modification of the magnetic structure of the Mn_5Si_3 alloy with Ni-doping at the Mn site [19]. However, the magnetic structure of other doped Mn_5Si_3 alloys has not yet been revealed. Significant changes in the magnetic properties have been noticed depending on the size and number of valance electrons in the dopant material [6,15,16].

In the present work, our aim is to focus on Cr-doped Mn_5Si_3 alloys of nominal compositions, $Mn_{5-x}Cr_xSi_3$ (for $x = 0.05, 0.1, \text{ and } 0.2$), and the effect of Cr-doping on the magnetic structure and probe their true doping status (substitutional or interstitial) through NPD studies and x-ray absorption spectroscopy (XAS), respectively. The larger size of Cr, compared to Mn, leads to the expansion of the lattice volume in Mn_5Si_3 alloy [6]. In contrast, Ni-doping causes a lattice volume contraction due to its smaller size [6,19]. Our NPD studies indicate the incorporation of Cr at the Mn2 site (containing most of the magnetic moments) of the alloy. This is notably different from the Ni-doping cases [19]. We also observed a relaxed change of magnetic structure with increasing Cr concentration compared to the Ni-doping case. Our x-ray absorption fine structure (XAFS) results confirm the substitutional character of Cr-doping. In addition, a significant variation of the XAFS patterns at different phases and with doping concentration has also been noticed.

II. EXPERIMENTAL DETAILS

Cr-doped polycrystalline Mn_5Si_3 alloys of nominal compositions, $Mn_{5-x}Cr_xSi_3$ ($x = 0.05, 0.1, \text{ and } 0.2$), were prepared by melting the required amount of constituent elements (purity $\geq 99.9\%$) in an inert argon atmosphere using a Centorr-make tri-arc furnace. The alloys were melted four times to achieve the desired homogeneity. The ingots were then sealed in evacuated quartz ampules and annealed at 900°C for seven days, followed by ice-water quenching. All the alloys were characterized through the room-temperature x-ray powder diffraction (XRD) technique (not shown here). The Cr concentrations $x = 0.05, 0.1, \text{ and } 0.2$ are equivalent to 1%, 2%, and 4% of doping, respectively, and we define these alloys as Cr1, Cr2, and Cr4. All the Cr-doped alloys were found to show $D8_8$ -type hexagonal structure at room temperature. No impurity phase has been detected in any of the alloys.

The NPD patterns at different constant temperatures were recorded using the POWGEN time-of-flight neutron diffractometer at Oak Ridge National Laboratory. Vanadium containers of 6 mm diameter were used to load the presently studied Cr-doped Mn_5Si_3 powder for the NPD studies. A POWGEN Automatic Changer (PAC) with the helium exchange gas environment was used to achieve the desired temperature of the measurement. Two neutron frames with center wavelengths 0.8 \AA and 2.667 \AA were used for the data collection. Previously reported neutron scattering length data (Mn $\rightarrow -3.73 \text{ fm}$, Cr $\rightarrow 3.63 \text{ fm}$, and Si $\rightarrow 4.15$

fm) confirmed the good neutron scattering character of the constituent elements [22]. The FULLPROF software package was used to refine the experimentally obtained NPD data [23]. The BASIREPS and VESTA software packages were used for magnetic symmetry analysis and creating magnetic structures, respectively [23–25].

To probe the local crystallographic structure around the Cr atoms, temperature-dependent (10–120 K) XAS measurements were performed around the Cr K absorption edge at the P65 beamline of the PETRA-III synchrotron source (DESY, Germany) [26]. The samples were placed on the sample holder using Kapton tape and the measurements were performed in fluorescence mode. Fluorescence-mode XAS spectra were acquired by employing an ionization chamber filled with appropriate gas to measure incoming beam intensity. Simultaneously, a passivated implanted planar silicon (PIPS) diode detector was positioned at 90° relative to the incoming x-ray beam, while the sample was mounted at 45° . For the reduction of higher harmonic contributions, the beam was collimated using a Si-coated mirror with an angle of incidence of 2 mrad. The spectrum of a Cr foil was used to calibrate the energy axis of the Si(111) double crystal monochromator. The first inflection point in the edge was calibrated to 5989 eV. A liquid helium flow cryostat was used to vary the temperature of the alloys. To improve the data statistics, several XAS spectra of Cr K -edge were recorded at each constant T . We used the open source DEMETER package (ATHENA and ARTEMIS) to process and analyze the x-ray absorption near-edge structure (XANES) and the extended x-ray absorption fine structure (EXAFS) parts of the acquired XAS data [27–31]. During the EXAFS analysis, the goodness-of-fit parameter was monitored continuously and it was kept between 1 and 3%.

III. EXPERIMENTAL RESULTS

A. Neutron powder diffraction

We conducted NPD measurements on all three Cr-doped Mn_5Si_3 alloys at 120 K, consistent with previous findings indicating paramagnetic (PM) ordering for these alloys at this temperature [6]. Such NPD patterns, along with the Rietveld refinement patterns, are presented in Figs. 1(a)–1(c) for Cr1, Cr2, and Cr4 alloys, respectively. The $D8_8$ -type hexagonal structure with $P6_3/mcm$ space group of these Cr-doped alloys has been identified through Rietveld refinement analyses of the recorded NPD data. All the samples were found to be free of any impurity phase. The absence of any magnetic reflection reconfirms the PM nature of all these Cr-doped alloys at 120 K. During the refinement, we tried to probe the distribution of Cr over the two available sites of Mn (Mn1 and Mn2). For all three doped alloys, we observed a slightly negative value of the occupancy parameter at the Mn1 site. Such behavior indicates that the doped Cr goes into the Mn2 site only. This is unlike the Ni-doped alloys, where Ni was found to go to the Mn1 site only [19]. The values of the hexagonal lattice parameters obtained for the presently studied Cr-doped alloys are found to be of the same order with pure and doped Mn_5Si_3 alloys [5,6,16,19,21]. The larger size of Cr results in a unidirectional

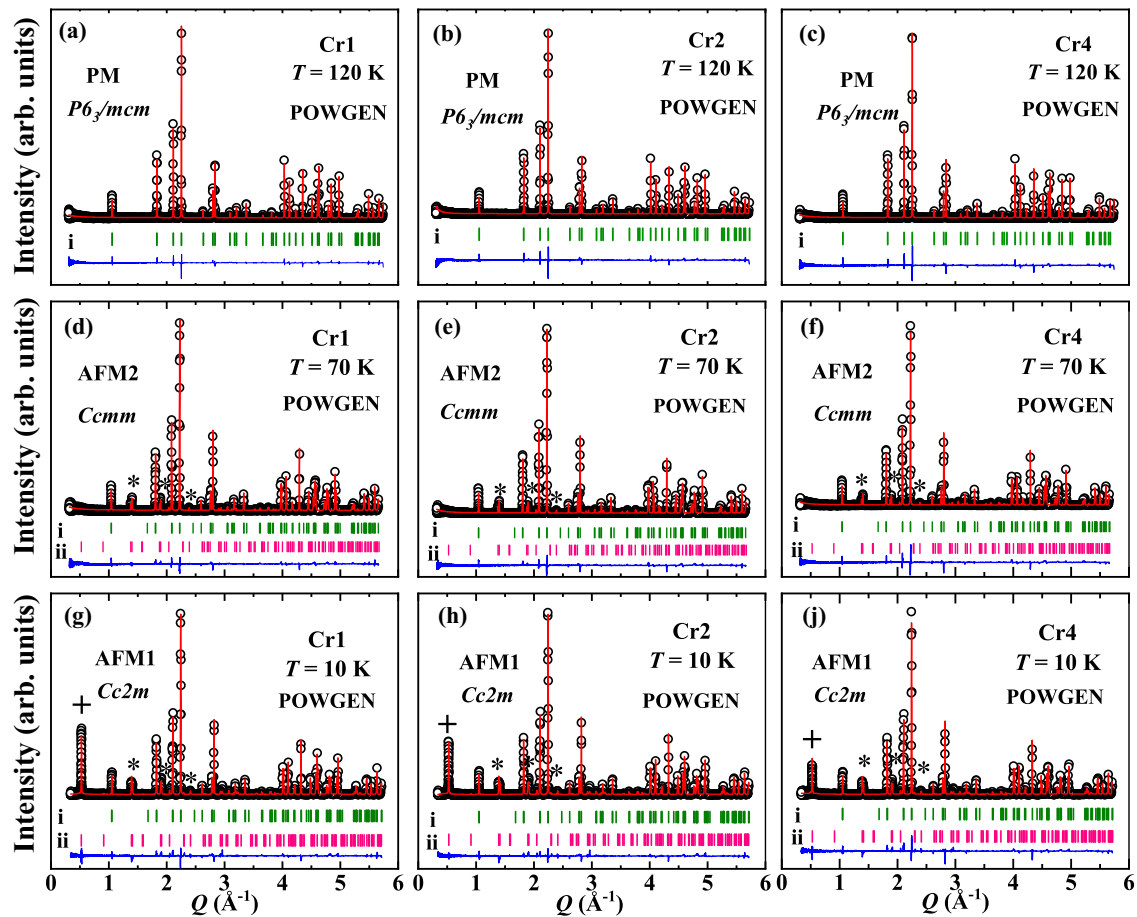


FIG. 1. 120, 70, and 10 K neutron powder diffraction patterns recorded in the POWGEN diffractometer along with calculated and difference patterns and Bragg's peak positions are plotted for Cr1 (a, d, and g), Cr2 (b, e, and h), and Cr4 (c, f, and j) alloys, respectively. Here, the black circles, red lines, and blue lines represent the observed, calculated, and difference patterns, respectively. The olive (labeled i) and magenta (labeled ii) vertical bars indicate the Bragg's peak positions for nuclear and magnetic reflections, respectively.

increase of hexagonal lattice parameters, and hence the lattice volume with doping concentration. All relevant refinement parameters, along with the lattice parameters, are given in Table I.

To investigate the effect of Cr-doping on the magnetic structure of AFM2 and AFM1 phases, we recorded the NPD data of all the Cr-doped alloys at 70 K (pure AFM2 phase) and 10 K (pure AFM1 phase). Figures 1(d)–1(f) depict the high-resolution NPD data recorded at 70 K, along with the Rietveld refinement patterns for Cr1, Cr2, and Cr4 alloys, respectively. These diffraction patterns are found to be markedly different from the 120 K patterns. Our analyses confirm the presence of orthorhombic distortion at 70 K. All the 70 K diffraction patterns were successfully refined by using the centrosymmetric $Ccmm$ orthorhombic space group. The orthorhombic and hexagonal lattice parameters are found to be correlated as $a_o \approx a_h$, $b_o \approx \sqrt{3}a_h$, and $c_o \approx c_h$. There are no indications of the high-temperature hexagonal phase being observed at 70 K. Some of the crystallographic sites of the hexagonal phase split into multiple sites, namely, (i) the Mn2 site splits into Mn21 and Mn22 sites, and (ii) the Si site splits into Si1 and Si2 sites. Notably, the Mn1 site remains unchanged. Such changes in nuclear structure and splitting

of crystallographic sites are consistent with the previously reported pure and doped Mn_5Si_3 alloys [1–4,9–14,19,21]. All relevant structural parameters at 70 K, obtained from the refinement, are depicted in Table I. Apart from the nuclear Bragg reflections, some additional peaks are also found to be associated with the NPD patterns (peaks with significant intensity have been indicated by an asterisk). Such reflections have been identified as magnetic reflections and successfully indexed by the commensurate propagation vector $q = (0, 1, 0)$. The allowed irreducible representations (IR) for the Mn sites of the presently studied alloys were determined through the magnetic symmetry analysis performed using the BASIREPS software package [23,24]. Such analysis indicates the presence of eight, six, and eight IRs for Mn1, Mn21, and Mn22 sites, respectively. Like the previously reported pure and Ni-doped alloys, refinement of magnetic diffraction intensity indicates the presence of ordered magnetic moment in the Mn22 site only [19]. Among the eight allowed IRs of the Mn22 site, only one IR (IR5) correctly replicates the observed intensities of the magnetic Bragg reflections. Our refinement indicates the ferromagnetically coupled basis vector (BV) along the a axis is zero (within the error bars) and a significant contribution from antiferromagnetically coupled

TABLE I. The refined structural parameters for $\text{Mn}_{4.95}\text{Cr}_{0.05}\text{Si}_3$ (Cr1), $\text{Mn}_{4.9}\text{Cr}_{0.1}\text{Si}_3$ (Cr2), and $\text{Mn}_{4.8}\text{Cr}_{0.2}\text{Si}_3$ (Cr4) alloys at 120, 70, and 10 K. Numbers in the brackets indicate the uncertainty in the last digit.

$\text{Mn}_{4.95}\text{Cr}_{0.05}\text{Si}_3$			$\text{Mn}_{4.9}\text{Cr}_{0.1}\text{Si}_3$			$\text{Mn}_{4.8}\text{Cr}_{0.2}\text{Si}_3$					
$T = 120 \text{ K}; \text{ space group} = P6_3/mcm$											
	a_h (Å)	c_h (Å)	γ (°)		a_h (Å)	c_h (Å)	γ (°)				
	6.859(9)	4.775(2)	120.00		6.887(0)	4.791(4)	120.00				
	R_p	R_{wp}	Bragg R -factor		R_p	R_{wp}	Bragg R -factor				
	10.4%	9.10%	6.28%		9.61%	9.36%	4.92%				
Atom	x	y	z	Atom	x	y	z	Atom	x	y	z
Mn1	0.333	0.667	0.000	Mn1	0.333	0.667	0.000	Mn1	0.333	0.667	0.000
Mn2/Cr-2	0.235(3)	0.000	0.250	Mn2/Cr-2	0.235(1)	0.000	0.250	Mn2/Cr-2	0.234(6)	0.000	0.250
Si	0.598(9)	0.000	0.250	Si	0.599(0)	0.000	0.250	Si	0.599(0)	0.000	0.250
$T = 70 \text{ K}; \text{ space group} = Ccmm$											
	a_o (Å)	b_o (Å)	c_o (Å)		a_o (Å)	b_o (Å)	c_o (Å)		a_o (Å)	b_o (Å)	c_o (Å)
	6.971(7)	12.014(9)	4.838(4)		6.972(5)	12.019(8)	4.837(1)		6.972(6)	12.024(4)	4.833(3)
	R_p	R_{wp}	Bragg R -factor		R_p	R_{wp}	Bragg R -factor		R_p	R_{wp}	Bragg R -factor
	11.9%	10.2%	6.08%		11.6%	10.8%	5.27%		12.6%	11.5%	7.37%
Atom	x	y	z	Atom	x	y	z	Atom	x	y	z
Mn1	0.000	0.333	0.000	Mn1	0.000	0.333	0.000	Mn1	0.000	0.333	0.000
Mn21/Cr21	0.236(0)	0.000	0.750	Mn21/Cr21	0.235(6)	0.000	0.750	Mn21/Cr21	0.234(7)	0.000	0.750
Mn22/Cr22	0.117(4)	0.117(6)	0.250	Mn22/Cr22	0.117(7)	0.117(7)	0.250	Mn22/Cr22	0.117(1)	0.117(1)	0.250
Si1	0.402(0)	0.000	0.250	Si1	0.401(6)	0.000	0.250	Si1	0.402(1)	0.000	0.250
Si2	0.201(6)	0.200(2)	0.750	Si2	0.200(6)	0.200(6)	0.750	Si2	0.201(8)	0.200(2)	0.750
$T = 10 \text{ K}; \text{ space group} = Cc2m$											
	a_o (Å)	b_o (Å)	c_o (Å)		a_o (Å)	b_o (Å)	c_o (Å)		a_o (Å)	b_o (Å)	c_o (Å)
	6.874(0)	11.969(0)	4.806(3)		6.875(0)	11.969(9)	4.803(4)		6.876(6)	11.970(9)	4.797(7)
	R_p	R_{wp}	Bragg R -factor		R_p	R_{wp}	Bragg R -factor		R_p	R_{wp}	Bragg R -factor
	11.7%	12.6%	4.53%		11.2%	12.9%	4.49%		13.1%	12.9%	6.24%
Atom	x	y	z	Atom	x	y	z	Atom	x	y	z
Mn11	0.000	0.333	0.000	Mn11	0.000	0.333	0.000	Mn11	0.000	0.333	0.000
Mn12	0.000	0.667	0.000	Mn12	0.000	0.667	0.000	Mn12	0.000	0.667	0.000
Mn21/Cr21	0.233(8)	0.000	0.750	Mn21/Cr21	0.233(9)	0.000	0.750	Mn21/Cr21	0.233(8)	0.000	0.750
Mn23/Cr23	0.118(4)	0.118(3)	0.250	Mn23/Cr23	0.117(9)	0.118(4)	0.250	Mn23/Cr23	0.118(0)	0.117(8)	0.250
Mn24/Cr24	0.881(5)	0.881(6)	0.750	Mn24/Cr24	0.882(0)	0.881(5)	0.750	Mn24/Cr24	0.881(9)	0.882(1)	0.750
Si1	0.401(0)	0.000	0.250	Si1	0.400(9)	0.000	0.250	Si1	0.401(4)	0.000	0.250
Si2	0.190(2)	0.204(9)	0.750	Si2	0.191(2)	0.203(4)	0.750	Si2	0.192(7)	0.203(0)	0.750
Si3	0.289(8)	0.303(5)	0.250	Si3	0.290(8)	0.302(1)	0.250	Si3	0.292(3)	0.301(1)	0.250

BV along the b axis. Such behavior results in a collinear AFM structure and matches well with the previously reported pure and doped Mn_5Si_3 alloys [9,10,19]. The collinear AFM structure obtained from our analysis is presented in Fig. 2(a) for the representative Cr4 alloy. The refinement parameters of the magnetic phase at 70 K for all the Cr-doped alloys are presented in Table II. The correctness of the magnetic structure refinement was further verified by analyzing the temperature-difference pattern of the 70 and 120 K data [see the Supplemental Material [32], Figs. S1(a), S1(b), and S1(c), for Cr1, Cr2, and Cr4 alloys, respectively].

We further recorded the NPD data for all the Cr-doped alloys at 10 K [see Figs. 1(g)–1(i)]. Such NPD data indicate additional changes in the nuclear and magnetic structures. Though the nuclear structure remains orthorhombic at 10 K, the structural space group becomes noncentrosymmetric $Cc2m$. Such change in structure results in the splitting of Mn1 and Mn22 sites. The Mn1 site splits into Mn11 and Mn12

sites; on the other hand, the Mn22 site splits into Mn23 and Mn24 sites. The Mn21 site remains unperturbed. Different structural parameters obtained after refinement are depicted in Table I. Apart from the nuclear structure change, additional magnetic reflections have also been observed. One such clearly visible additional magnetic reflection has been marked with a + sign in Figs. 1(g)–1(i). Similar to the collinear phase, the observed magnetic reflections at 10 K can also be successfully indexed by the commensurate propagation vector $q = (0, 1, 0)$. However, none of the IRs [four IRs for each of the five available Mn sites (Mn11, Mn12, Mn21, Mn23, and Mn24)] obtained from the symmetry analysis can replicate the intensities of the magnetic reflections observed at 10 K. We observed a complete mixing of the IRs. Similar behavior has been observed for other doped Mn_5Si_3 alloys as well [9,10,13,19]. Solyom *et al.* already explained that the symmetry analysis is no longer supported by Landau theory for first-order transitions, such as $P6_3/mcm \rightarrow Ccmm \rightarrow Cc2m$

TABLE II. The refinement results for the magnetic structures of $\text{Mn}_{4.95}\text{Cr}_{0.05}\text{Si}_3$ (Cr1), $\text{Mn}_{4.9}\text{Cr}_{0.1}\text{Si}_3$ (Cr2), and $\text{Mn}_{4.8}\text{Cr}_{0.2}\text{Si}_3$ (Cr4) alloys at 70 and 10 K. We have used Cartesian and spherical descriptions for 70 and 10 K refinement, respectively.

$\text{Mn}_{4.95}\text{Cr}_{0.05}\text{Si}_3$				$\text{Mn}_{4.9}\text{Cr}_{0.1}\text{Si}_3$				$\text{Mn}_{4.8}\text{Cr}_{0.2}\text{Si}_3$			
$T = 70 \text{ K}$											
Atom	$M (\mu_B)$			Atom	$M (\mu_B)$			Atom	$M (\mu_B)$		
Mn22				Mn22				Mn22			
(0.1174, 0.1177, 0.25)	1.28(7)			(0.1177, 0.1177, 0.25)	1.26(1)			(0.1171, 0.1173, 0.25)	1.21(7)		
(0.8826, 0.1177, 0.75)	1.28(7)			(0.8822, 0.1177, 0.75)	1.26(1)			(0.8829, 0.1173, 0.75)	1.21(7)		
(0.3826, 0.3823, 0.75)	1.28(7)			(0.3822, 0.3822, 0.75)	1.26(1)			(0.3829, 0.3827, 0.75)	1.21(7)		
(0.6174, 0.3823, 0.25)	1.28(7)			(0.6177, 0.3822, 0.25)	1.26(1)			(0.6171, 0.3827, 0.25)	1.21(7)		
$T = 10 \text{ K}$											
Atom	$M (\mu_B)$	ϕ°	θ°	Atom	$M (\mu_B)$	ϕ°	θ°	Atom	$M (\mu_B)$	ϕ°	θ°
Mn11				Mn11				Mn11			
(0.00, 0.3333, 0.00)	0.75(2)	90	136(1)	(0.00, 0.3333, 0.00)	0.78(5)	90	137(3)	(0.00, 0.3333, 0.00)	0.84(3)	90	141(5)
(0.00, 0.3333, 0.50)	0.75(2)	90	136(1)	(0.00, 0.3333, 0.50)	0.78(5)	90	137(3)	(0.00, 0.3333, 0.50)	0.84(3)	90	141(5)
Mn12				Mn12				Mn12			
(0.00, 0.6666, 0.00)	-0.75(2)	90	136(1)	(0.00, 0.6666, 0.00)	-0.78(5)	90	137(3)	(0.00, 0.6666, 0.00)	-0.84(3)	90	141(5)
(0.00, 0.6666, 0.50)	-0.75(2)	90	136(1)	(0.00, 0.6666, 0.50)	-0.78(5)	90	137(3)	(0.00, 0.6666, 0.50)	-0.84(3)	90	141(5)
Mn23				Mn23				Mn23			
(0.1185, 0.1184, 0.25)	1.27(9)	90	69(1)	(0.1179, 0.1184, 0.25)	1.29(9)	90	61(1)	(0.1181, 0.1179, 0.25)	1.33(9)	90	60(3)
(0.8815, 0.1184, 0.75)	-1.27(9)	90	69(1)	(0.8820, 0.1174, 0.75)	-1.29(9)	90	61(1)	(0.8819, 0.1179, 0.75)	-1.33(9)	90	60(3)
Mn24				Mn24				Mn24			
(0.1185, 0.8816, 0.25)	-1.61(6)	90	49(2)	(0.1179, 0.8816, 0.25)	-1.59(1)	90	50(2)	(0.1181, 0.8821, 0.25)	-1.53(1)	90	52(3)
(0.8815, 0.8816, 0.75)	1.61(6)	90	49(2)	(0.8820, 0.8816, 0.75)	1.59(1)	90	50(2)	(0.8819, 0.8821, 0.75)	1.53(1)	90	52(3)

[33]. To finalize the magnetic phase refinement at 10 K, we used spherical coordinates and followed the similar procedure

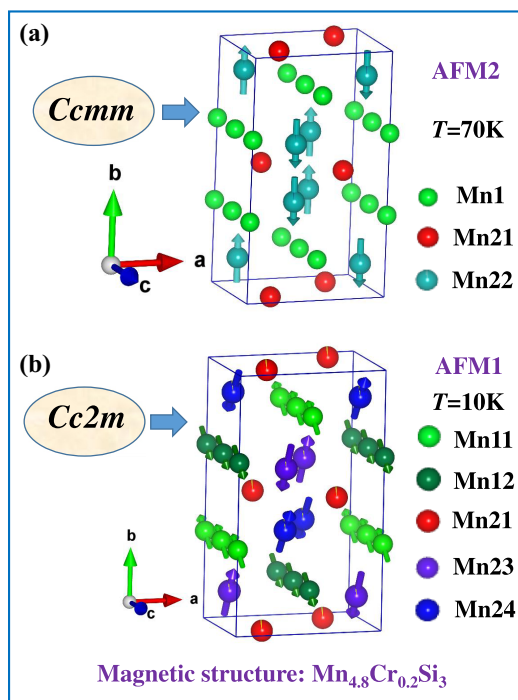


FIG. 2. The collinear and noncollinear antiferromagnetic structures at (a) 70 K and (b) 10 K for Cr4 alloy, respectively.

adopted for the Ni-doped alloys [19]. The final magnetic refinement parameters obtained for the presently studied Cr-doped alloys are presented in Table II. We have also plotted the magnetic structure of this $Cc2m$ phase achieved from our refinement analysis in Fig. 2(b). Due to the low symmetry of the system, the solution may not be claimed to be the unique one. We reported a similar solution for the Ni-doped alloys [19]. However, Biniskos *et al.* reported three possible solutions for the undoped Mn_5Si_3 alloy [14]. Different magnetic refinement parameters [magnetic moment size, spherical angle θ (angle between c axis and ab plane)] obtained from the analysis match well with the previously reported pure and doped Mn_5Si_3 alloys [9,10,19]. Among five different Mn sites, the Mn21 site does not show any magnetic order. The solution obtained in the present case was further confirmed by refining the temperature-difference pattern of the 10 and 120 K data [see the Supplemental Material [32], Figs. S1(d), S1(e), and S1(f), for Cr1, Cr2, and Cr4 alloys, respectively].

B. X-ray absorption spectroscopy

To gain further insight into the local environment surrounding the Cr atoms, we conducted XAS measurements at different constant T around the Cr K absorption edge for all three Cr-doped alloys. Figures 3(a)–3(c) display the normalized XANES spectra at the Cr K -edges recorded at different constant T for Cr1, Cr2, and Cr4 alloys, respectively. The Cr foil reference data have also been plotted in Fig. 3(a), along with 120 K data. Here, the normalized intensities at different compositions at a particular T are vertically shifted for

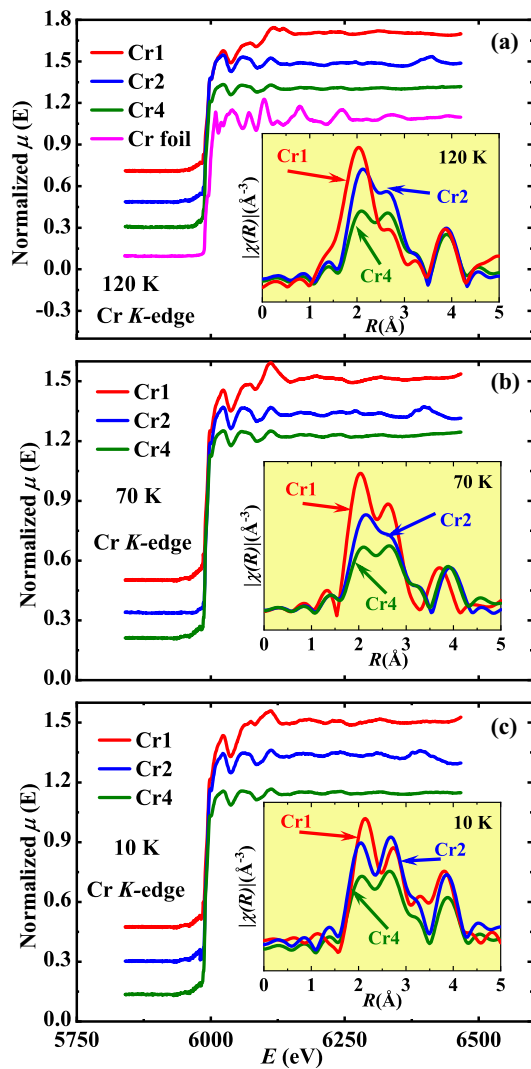


FIG. 3. The normalized XANES spectra of Cr1, Cr2, and Cr4 alloys, at 120, 70, and 10 K, respectively, for Cr *K*-edges. Insets: the comparison between FT of EXAFS signals (extracted from EXAFS signal), as a function of distance from the active site for Cr1, Cr2, and Cr4 alloys.

better visualization. Similar edge energies (~ 5989 eV) were observed for all the doped alloys at different T regions and the absence of any pre-edge transition confirms the elemental (zero oxidation) state of the metals in these alloys.

To shed more light on the local atomic structure and its possible modification around the AFM1 \rightarrow AFM2 \rightarrow PM transitions, T -dependent Cr *K*-edge EXAFS measurements were performed. For local structure analysis, we performed necessary preprocessing in ATHENA and extracted EXAFS data [$k^2\chi(k)$ vs k], where k is defined as $k = \sqrt{\frac{2m(E-E_0)}{\hbar^2}}$. We further Fourier transformed (FT) the EXAFS signal into radial distance (R) space and used $\chi(R)$ vs R data for theoretical analysis. During the FT of the EXAFS signal, we restricted the k range between 2.5 \AA^{-1} and 10 \AA^{-1} to eliminate the high- k region with a poor signal-to-noise ratio. Modulus of such FT EXAFS data, recorded at the Cr *K*-edges, for all three Cr-doped alloys at different constant T

are plotted in Fig. 4. The EXAFS equation is defined as $\chi(k) = \sum_j \frac{S_0^2 N_j f_j(k) e^{-2k^2\sigma_j^2}}{kR_j^2} \sin[2kR_j + \delta_j(k)]$, where R_j refers to the radial distance to the j th neighboring atom, N_j refers to the coordination number of the j th neighboring atom, σ_j^2 is the Debye-Waller factor (which gives the mean-square fluctuations in the bond distances), δ_j is the phase factor, and S_0^2 refers to the passive electron amplitude reduction factor [28,29,34–36]. The theoretical fitting curves of the $\chi(R)$ versus R plots were generated by using the structural parameters (e.g., space group, lattice parameters, and Wyckoff positions of the atoms) obtained from our NPD refinement. During the analysis of these EXAFS data, the fitting parameters (such as amplitude reduction factor, Debye-Waller factor, and change in path length) were independently varied for each single scattering (SS) path by keeping the coordination numbers unchanged. Here, we assumed that the coordination numbers for each path were accurately defined through our NPD analysis, as we have not observed any additional phase in any of the presently studied alloys at any temperature.

The inset of Fig. 3(a) represents the comparison between FT [$\chi(R)$ vs R plots] of the 120 K EXAFS signal for all the doped alloys. This comparison indicates that there is a noticeable variation in the pattern for different compositions. The fitting curves of these $\chi(R)$ vs R plots (both real and imaginary parts), obtained using the FEFF-6 code, are plotted in Figs. 4(a)–4(c) for Cr1, Cr2, and Cr4 alloys, respectively. The ATOMS program was employed to prepare the inputs for FEFF [27]. Subsequently, the FEFFIT program was utilized to fit the experimental data [28–31]. The scattering amplitudes and phase shifts are calculated using the FEFF program [28–31]. In order to generate the scattering paths for samples with different Cr concentrations, the Mn atoms in the FEFF code input were replaced by the Cr atoms according to the structural occupancies. Our NPD analysis confirmed the presence of two inequivalent Mn sites (Mn1 and Mn2) at 120 K and the incorporation of Cr atoms in the Mn2 site only. To further confirm such Cr-atom occupancy, we repeated the entire fitting procedure by incorporating Cr atoms in each Mn site. However, the value of the amplitude reduction factor S_0^2 is found to be significantly low (~ 0.3) and unacceptable if we put Cr atoms in the Mn1 site. On the other hand, incorporation of Cr atoms in the Mn2 site results in an acceptable value of S_0^2 , which is ~ 0.8 [36]. Such observation further confirms the presence of doped Cr atoms in the Mn2 site only. The k -space fitting data of the EXAFS signal at 120 K, along with different path contributions, are plotted in Figs. 5(a)–5(c) for Cr1, Cr2, and Cr4 alloys, respectively. Taking the instrument's resolution into consideration, we merged the scattering paths of similar R values (within $\sim 0.1 \text{ \AA}$) for similar types of atoms [37,38]. The path contributions have been vertically adjusted for better visualization. The representation of path contributions as depicted in Fig. 5 can be explained in the following manner: e.g., in the case of Si1.1 SS 2.439 $\sigma^2 = 0.00122(3)$, Si1 represents the scattering atom symbol, the next number (1 in the present case) denotes the shell number of the atom (in this case, Si) from where the ejected core electron is scattered (1 means first Si atom shell around the central Cr

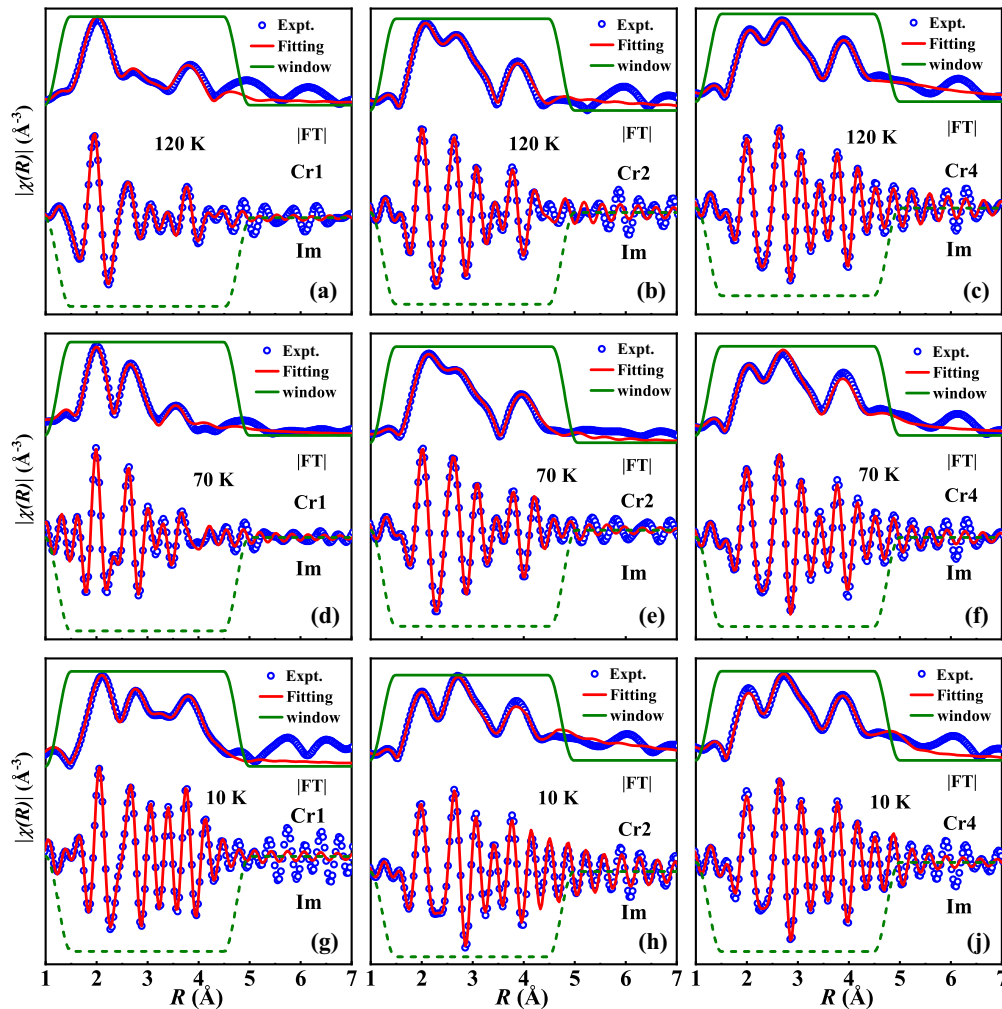


FIG. 4. The Fourier transforms of the k^2 weighted EXAFS data (blue circles) and the corresponding best fitted curve (solid red line); the magnitude ($|FT|$) and the imaginary parts (Im) are indicated and are vertically shifted for clarity for (a), (d), (g) Cr1, (b), (e), (h) Cr2, and (c), (f), (j) Cr4 alloys, respectively, at different constant temperature for Cr K -edges. The Hanning window function is represented by the solid and dashed olive lines.

atom, 2 means second shell and so on), SS indicates the single scattering path, the next set of numbers (2.439 in Å) indicates the distance at which the scatterer is located from the central Cr atom, and, in the last part, the value of σ^2 (in Å²) represent the thermal and structural disorder of that particular path [37,38]. A comparison of Figs. 5(a) and 4(a) clearly reveals that the main contributions for the first coordination shell are coming from the Cr-Si1 (nearest-neighbor) path and Cr-Si1 (next-nearest-neighbor) path ($N = 3$ and 2, respectively), the second coordination shell arises due to the Cr-Mn2/Cr (nearest-neighbor) path and Cr-Mn1 (nearest-neighbor) path ($N = 6$ and 4, respectively), and for the third coordination shell, there are several contributions: the Cr-Mn2/Cr (next-nearest-neighbor) path, Cr-Si3 (next to next-nearest-neighbor) path, Cr-Mn2/Cr (next to next-nearest-neighbor) path, and Cr-Mn1 (next-nearest-neighbor) path ($N = 2, 4, 2,$ and 4, respectively), as the first three dominant positions appear at 2.00, 2.73, and 3.85 Å [see Fig. 4(a)]. Notably, a significant variation in the peak shape and position has also been no-

ticed with increasing Cr concentration [see Figs. 4(a)–4(c)]. Figure 5 further supports such observations (clear from different path contributions). The observed systematic increase in the second and third coordination shells is probably due to the presence of Cr in those shells.

Similar analyses have also been carried out at 70 and 10 K EXAFS data for all three alloys. Monotonic variation of the FT of the EXAFS signals at both of the T 's was noticed with the doping concentration [see insets of Figs. 3(b) and 3(c)]. All of the fitting curves are depicted in Figs. 4(d)–4(j). Careful observation reveals that the dominant peak positions become closer with a decrease in the sample T as the coordination shells become closer (see Fig. 4). In addition, the second coordination shell was also found to be getting more prominent with decreasing alloy temperature. Interestingly, such an effect becomes slower with increasing doping concentration. The observed decrease in coordination shell positions shows a one-to-one correspondence with the lattice parameters obtained from the NPD analysis (see Table I).

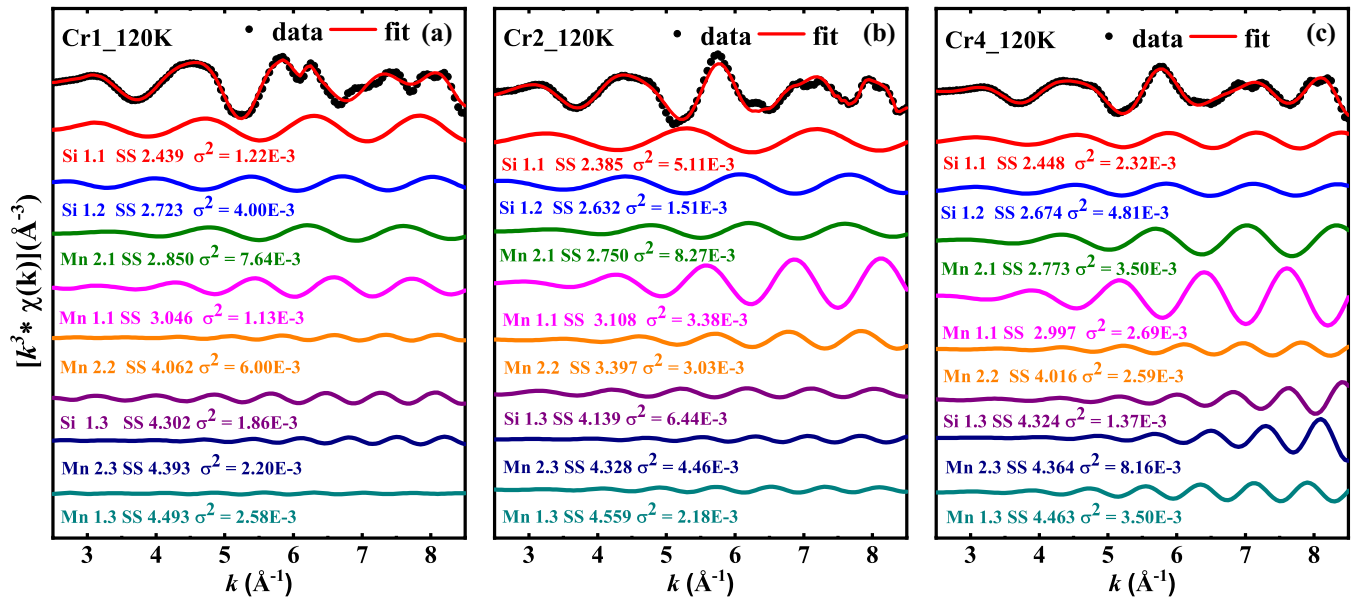


FIG. 5. The Cr K -edges k^3 weighted experimental EXAFS data in k -space (black circles) at $T = 120$ K and the corresponding best fit (red solid line) for (a) Cr1, (b) Cr2, and (c) Cr4 alloys, respectively. The individual fitted paths are shifted below for better visualization, giving the scatterer, distance from the active site, and corresponding Debye-Waller factor. For better visualization of the scattering path mechanism, we have not included the residual path contribution in the above figures.

IV. DISCUSSION AND CONCLUSIONS

A systematic investigation of the nuclear and magnetic structure of three Cr-doped Mn_5Si_3 alloys of nominal compositions, $\text{Mn}_{5-x}\text{Cr}_x\text{Si}_3$ (for $x = 0.05, 0.1, \text{ and } 0.2$), were performed through detailed NPD and XAS studies. Our results unfold several crucial effects of Cr-doping on the nuclear and magnetic structures of this material. All the Cr-doped alloys are found to crystallize with $D8_8$ -type hexagonal structure (space group $P6_3/mcm$), and the structures remain unchanged until the PM \rightarrow AFM2 transition at 100 K. Such behavior is confirmed by the observation of the hexagonal structures of the materials at 120 K from the NPD data. The hexagonal lattice parameters were found to show a monotonic increase with increasing doping concentration, confirming the Vegard's law. The Rietveld refinement analysis also confirms the incorporation of Cr atoms in the Mn2 sites of the material. This is unlike the Ni-doping cases, where the doped Ni atoms were found to go to the Mn1 sites instead of the Mn2 sites of the alloy [19]. Such behavior may be related to the larger size of the dopant Cr atoms for the presently studied alloys. The incorporation of Cr atoms in the Mn2 sites has a larger impact on the magnetic structure as the majority of the magnetic contributions come from the Mn2 site in low- T AFM1 and AFM2 phases. The doped alloys undergo two magnetostructural transitions [6], which are clear from the observation of two completely different structures at 70 and 10 K. The nuclear structure at 70 K is found to be orthorhombic in nature with space group $Cmcm$. Notably, splitting in the Mn2 site (Mn21 and Mn22), which is similar to pure and Ni-doped alloys, has been observed [19]. Cr-doping results in a significant amount of change in the Mn22 moment size. For a 4% change in the Cr concentration, about an 18.2% decrease in the Mn22 moment size has been observed (Mn22 site moment size for undoped Mn_5Si_3 alloy is $1.48(1)\mu_B$ [11]).

This is unlike the doping of Ni in the Mn site, where only about a 5.4% decrease in moment size has been observed [19]. The presence of Cr in the magnetically ordered Mn2 site (instead of the nonmagnetic Mn1 site observed for the Ni-doping case) is mainly responsible for such a large decrease in the Mn22 moment size.

The NPD data at 10 K further confirm the presence of another type of structural change in the Cr-doped alloys. The orthorhombic space group becomes $Cc2m$ (noncentrosymmetric type) at 10 K along with splitting in the available Mn sites. In addition to the change in the orthorhombic space group, a strong distortion in the orthorhombic lattice parameters has also been noticed. The distortion of the pseudo hexagonal lattice parameters ($a_o\sqrt{3}/b_o$) in the AFM2 and AFM1 phases is $\sim 1.004(3)$ and $0.994(2)$, respectively, for all three Cr-doped alloys. Apart from that, a large change in the orthorhombic lattice parameter c_o has also been noticed. Notably, the nature of the observed distortion in the lattice parameters is markedly different from the Ni-doped alloys, where a gradual reduction in the distortion has been observed with increasing Ni concentration [19]. The presence of Cr in the Mn2 site instead of the Mn1 site (observed in the case of Ni-doping) results in a significant change in the behavior of moment size with increasing doping concentration. We observed an increasing trend in the moment sizes for Mn1 (Mn11 and Mn12) and Mn23 sites. For Cr concentration changing from 1 to 4%, $\sim 12\%$ and $\sim 4.7\%$ increase in moment size have been observed for Mn1 and Mn23 sites, respectively. On the other hand, the Mn24 site shows $\sim 4.9\%$ decrease in moment size for a similar change in Cr concentration. Notably, for the Ni-doping case, the Mn1 site (Mn11 and Mn12) moment size shows a monotonic decrease with increasing doping concentration [19]. Such behavior is not unexpected as the Mn1 site remains unperturbed for the presently studied Cr-doping cases. The angle between the c

axis and ab plane, θ , shows an increasing trend (unlike the Ni-doping case) for the Mn1 sites. However, θ values of Mn23 and Mn24 sites were found to approach each other for a near-parallel arrangement.

The presence of multiple exchange interactions (six for the AFM1 phase and four for the AFM2 phase) has recently been predicted in various theoretical models by several research groups [2–4,14]. Such exchange interactions strongly depend on the intra- and intersite distances of Mn atoms. Our NPD analysis confirms a significant change in the Mn-Mn distance with increasing Cr concentration: (i) a monotonic decrease in intrasite Mn1-Mn1 distance [from 2.403(4) Å in Cr1 to 2.402(1) Å and 2.398(9) Å for Cr2, and Cr4 at 10 K], (ii) a monotonic decrease in intrasite Mn2-Mn2 distance [e.g., at 10 K, Mn23-Mn23 distance = 2.906(7) Å, 2.901(1) Å, 2.899(3) Å for Cr1, Cr2, and Cr4 alloys, respectively], and (iii) a monotonic increase in intersite Mn24-Mn1 distance [e.g., at 10 K, distance = 2.942(1) Å, 2.945(3) Å, 2.946(2) Å for Cr1, Cr2, and Cr4 alloys, respectively]. Intrasite Mn2-Mn2 distance shows a clear contrast when compared with the Ni-doping cases [19]. Such contrast may play a pivotal role in the slower decrease of T_{N1} with increasing Cr concentration. On the other hand, approaching parallel arrangement of the Mn23 and Mn24 site moments with increasing Cr concentration is another important observation of the present study. Nonparallel arrangements of Mn23 and Mn24 moments are mainly responsible for the appearance of the AFM1' phase in pure and doped Mn₅Si₃ alloys, which plays a pivotal role behind the observed unusual properties such as IHL, AHE, TI, etc. [1,5,6,19]. Cr-doping induced parallel arrangement of Mn23 and Mn24 moments results in a gradual disappearance of such unusual properties in the presently studied alloys [6].

The role of structural disorder is anticipated to be pivotal in shaping the physical response of complex systems, potentially influencing various properties [34,35,37,39–41]. Concerning the investigation of the intricate local crystallographic structure, our EXAFS studies reveal two noteworthy trends of variation. One trend is linked to the concentration of Cr, while the other is influenced by the alloy T . As the concentration of Cr increases, the contribution of bonds containing Cr in the second coordination shell demonstrates a consistent rise compared to bonds lacking Cr in the first coordination shell across the entire T range. In the case of the Cr1 alloy, bonds within the first coordination shell progressively contribute more to shaping the local environment of Cr with rising temperature. However, the other two studied samples exhibit temperature-independent behavior in this aspect. These findings indicate that from a quantitative perspective, all the EXAFS signals display similar characteristics across all

compositions despite notable differences observed in the first and second coordination shells around the central absorbing Cr atom. The presence of the Cr atom in the magnetic Mn site (i.e., Mn2 site) significantly influences the scattering path associated with the second coordination shell, playing a crucial role in the manifestation of the observed unusual properties. Despite encountering multiple first-order structural transitions and a complex magnetic environment, a substantial degree of local crystallographic structure consistently persists in the compositions.

In summary, our comprehensive investigation utilizing detailed NPD and XAFS techniques provides insights into the magnetic structure and Cr-local environments within all three Cr-doped Mn₅Si₃ alloys. These studies confirm the integration of Cr atoms into the magnetic Mn2 sites. While both collinear (AFM2) and noncollinear (AFM1) phases are observed in all doped alloys, Cr-doping induces significant alterations in the magnetic structures of both phases. The noncollinear alignment of the Mn23 and Mn24 magnetic moments tends toward a near-parallel configuration with increasing Cr concentration, directly influencing the emergence of the AFM1' phase under external magnetic fields. This near-parallel alignment suggests a preference for the AFM2 phase over the AFM1 phase in Cr-doped alloys, consequently reducing the magnetic transition temperature, denoted as T_{N1} . Furthermore, the bonds within the first coordination shell increasingly contribute to shaping the local environment of Cr with rising temperature in the Cr1 sample, while the other two samples exhibit temperature-independent behavior.

ACKNOWLEDGMENTS

S.C. and R.R. would like to thank the Science and Engineering Research Board (SERB), DST-India, for financial support (Project No. CRG/2020/000670). J.S. would also like to thank SERB, DST-India, for the Ramanujan Fellowship [Grant No. RJF/2019/000046 (SQUID-1986-JS-3632)]. A portion of this research used resources at the Spallation Neutron Source (Proposal No. IPTS-31093), a U.S. Department of Energy Office of Science User Facility operated by the Oak Ridge National Laboratory. The entire POWGEN team is hereby acknowledged for their help in recording the NPD data. A portion of this research was carried out at the light source PETRA III of DESY (Proposal No. I-20211204), a member of the Helmholtz Association (HGF). Financial support by the Department of Science and Technology (Government of India) provided within the framework of the India@DESY collaboration is gratefully acknowledged.

- [1] C. Sürgers, T. Wolf, P. Adelman, W. Kittler, G. Fischer, and H. V. Löhneysen, *Sci. Rep.* **7**, 42982 (2017).
- [2] N. Biniskos, K. Schmalzl, S. Raymond, S. Petit, P. Steffens, J. Persson, and T. Brückel, *Phys. Rev. Lett.* **120**, 257205 (2018).
- [3] N. Biniskos, F. J. dos Santos, M. dos Santos Dias, S. Raymond, K. Schmalzl, P. Steffens, J. Persson, N. Marzari, S. Blügel, S. Lounis, and T. Brückel, *APL Mater.* **11**, 081103 (2023).

- [4] F. J. dos Santos, N. Biniskos, S. Raymond, K. Schmalzl, M. dos Santos Dias, P. Steffens, J. Persson, S. Blügel, S. Lounis, and T. Brückel, *Phys. Rev. B* **103**, 024407 (2021).
- [5] S. C. Das, K. Mandal, P. Dutta, S. Pramanick, and S. Chatterjee, *Phys. Rev. B* **100**, 024409 (2019).
- [6] S. C. Das, K. Mandal, N. Khamaru, S. Pramanick, and S. Chatterjee, *J. Phys.: Condens. Matter* **32**, 485802 (2020).

- [7] M. Gottschilch, O. Gourdon, J. Persson, C. de la Cruz, V. Petricek, and T. Brueckel, *J. Mater. Chem.* **22**, 15275 (2012).
- [8] H. J. Al-Kanani and J. G. Booth, *J. Magn. Magn. Mater.* **140–144**, 1539 (1995).
- [9] P. J. Brown, J. B. Forsyth, V. Nunez, and F. Tasset, *J. Phys.: Condens. Matter* **4**, 10025 (1992).
- [10] P. J. Brown and J. B. Forsyth, *J. Phys.: Condens. Matter* **7**, 7619 (1995).
- [11] M. R. Silva, P. J. Brown, and J. B. Forsyth, *J. Phys.: Condens. Matter* **14**, 8707 (2002).
- [12] G. H. Lander, P. J. Brown, and J. B. Forsyth, *Proc. Phys. Soc.* **91**, 332 (1967).
- [13] A. Z. Menshikov, A. P. Vokhmyanin, and Y. A. Dorofeev, *Phys. Stat. Solidi (b)* **158**, 319 (1990).
- [14] N. Biniskos, F. J. dos Santos, K. Schmalzl, S. Raymond, M. dos Santos Dias, J. Persson, N. Marzari, S. Blügel, S. Lounis, and T. Brückel, *Phys. Rev. B* **105**, 104404 (2022).
- [15] S. C. Das, S. Pramanick, and S. Chatterjee, *J. Magn. Magn. Mater.* **529**, 167909 (2021).
- [16] S. C. Das and S. Chatterjee, *J. Alloys Compd.* **892**, 162212 (2022).
- [17] Songlin, Dagula, O. Tegus, E. Brück, J. C. P. Klaasse, F. R. de Boer, and K. Buschow, *J. Alloys Compd.* **334**, 249 (2002).
- [18] H. J. Al-Kanani and J. G. Booth, *J. Appl. Phys.* **81**, 4152 (1997).
- [19] S. K. Adhikari, R. Roy, S. C. Das, J. Sannigrahi, S. Pramanick, S. Chattopadhyay, C. Ritter, D. T. Adroja, and S. Chatterjee, *J. Alloys Compd.* **967**, 171752 (2023).
- [20] M. A. Haddouch, N. Abboushi, N. Sharma, A. Eich, A. Grzechnik, C. Li, M. Tolkiehn, H. Alsamamra, J. Voigta, and K. Friese, *J. Appl. Crystallogr.* **55**, 1164 (2022).
- [21] S. K. Adhikari, R. Roy, S. C. Das, S. Pramanick, K. De, O. Ivashko, A.-C. Dippel, M. v. Zimmermann, S. Bandyopadhyay, and S. Chatterjee, *J. Magn. Magn. Mater.* **589**, 171591 (2024).
- [22] V. F. Sears, *Neutron News* **3**, 26 (1992).
- [23] J. Rodríguez-Carvajal, *Phys. B: Condens. Matter* **192**, 55 (1993).
- [24] C. Ritter, *Solid State Phenomena* **170**, 263 (2011).
- [25] K. Momma and F. Izumi, *J. Appl. Crystallogr.* **44**, 1272 (2011).
- [26] E. Welter, R. Chernikov, M. Herrmann, and R. Nemausat, *AIP Conf. Proc.* **2054**, 040002 (2019).
- [27] B. Ravel, *J. Synchrotron Radiat.* **8**, 314 (2001).
- [28] S. I. Zabinsky, J. J. Rehr, A. Ankudinov, R. C. Albers, and M. J. Eller, *Phys. Rev. B* **52**, 2995 (1995).
- [29] M. Newville, *J. Synchrotron Radiat.* **8**, 322 (2001).
- [30] B. Ravel and M. Newville, *J. Synchrotron Radiat.* **12**, 537 (2005).
- [31] B. Ravel and M. Newville, *Phys. Scr.* **2005**, 1007 (2005).
- [32] See Supplemental Material at <http://link.aps.org/supplemental/10.1103/PhysRevMaterials.8.064405> for difference patterns of (i) 70 and 120 K, (ii) 10 and 120 K neutron diffraction patterns for Cr1, Cr2, and Cr4 alloys.
- [33] J. Solyom, *J. Phys. Colloques* **32**, C1 (1971).
- [34] D. Rani, J. Kangsabanik, K. G. Suresh, N. Patra, D. Bhattacharyya, S. N. Jha, and A. Alam, *Phys. Rev. Appl.* **10**, 054022 (2018).
- [35] B. Ravel, M. P. Raphael, V. G. Harris, and Q. Huang, *Phys. Rev. B* **65**, 184431 (2002).
- [36] H. Husain, M. Sulthonul, B. Hariyanto, C. Cholsuk, and S. Pratapa, *Mater. Today: Proc.* **44**, 3296 (2021).
- [37] M. Das, S. Bhowal, J. Sannigrahi, A. Bandyopadhyay, A. Banerjee, G. Cibir, D. Khalyavin, N. Banerjee, D. Adroja, I. Dasgupta, and S. Majumdar, *Phys. Rev. B* **105**, 134421 (2022).
- [38] M. Numan, G. Das, P. Dutta, M. Das, G. Manna, S. Giri, G. Aquilanti, and S. Majumdar, *J. Phys. Chem. Solids* **184**, 111712 (2024).
- [39] S. Wurmehl, G. H. Fecher, H. C. Kandpal, V. Ksenofontov, C. Felser, H.-J. Lin, and J. Morais, *Phys. Rev. B* **72**, 184434 (2005).
- [40] S. Malik, E. Dias, A. Nigam, and K. Priolkar, *J. Phys. D: Appl. Phys.* **55**, 165002 (2022).
- [41] C. Meneghini, S. Ray, F. Liscio, F. Bardelli, S. Mobilio, and D. D. Sarma, *Phys. Rev. Lett.* **103**, 046403 (2009).